Reduced Order Modeling Inversion of Monostatic Data in a Multi-scattering Environment*

Vladimir Druskin[†], Shari Moskow[‡], and Mikhail Zaslavsky[§]

Abstract. Data-driven reduced order models (ROMs) have recently emerged as an efficient tool for the solution of inverse scattering problems with applications to seismic and sonar imaging. One requirement of this approach is that it uses the full square multiple-input/multiple-output (MIMO) matrix-valued transfer function as the data for multidimensional problems. The synthetic aperture radar (SAR), however, is limited to the single-input/single-output (SISO) measurements corresponding to the diagonal of the matrix transfer function. Here we present a ROM-based Lippmann–Schwinger approach overcoming this drawback. The ROMs are constructed to match the data for each source-receiver pair separately, and these are used to construct internal solutions for the corresponding source using only the data-driven Gramian. Efficiency of the proposed approach is demonstrated on 2D and 2.5D (3D propagation and 2D reflectors) numerical examples. The new algorithm not only suppresses multiple echoes seen in the Born imaging but also takes advantage of their illumination of some back sides of the reflectors, improving the quality of their mapping.

Key words. inverse scattering, reduced order models, Lippmann–Schwinger, synthetic aperture radar, monostatic

MSC codes. 78A46, 65M32, 35R30

DOI. 10.1137/23M1564365

1. Introduction. The reduced order model (ROM) approach has been shown previously to be a powerful tool for inverse impedance, scattering, and diffusion [3, 7, 17, 16, 8, 9, 6, 5, 18, 14, 19, 11]. In this work, we apply it via the Lippmann–Schwinger–Lanczos algorithm [18] to models of synthetic aperture radar (SAR). In the process, we present a simplification of the ROM approach that applies for general time domain problems. This simplification both makes the algorithm and its exposition more direct and yields potential for computational speedup.

In the ROM framework for solving multidimensional inverse problems, given a full symmetric matrix transfer function, the ROM is chosen precisely to match the given data set; see

Funding: This material is partially based upon work supported by the NSF grant DMS-1929284 while the authors were in residence at the ICERM in Providence, RI, during the Spring 2020 Semester Program "Model and dimension reduction in uncertain and dynamic systems" and the Spring 2020 Reunion Event. The first author was partially supported by AFOSR grants FA 955020-1-0079, FA9550-20-1-0079, and NSF grant DMS-2110773. The third author was partially supported by AFOSR grant FA9550-20-1-0079. The second author was partially supported by NSF grant DMS-2008441.

^{*}Received by the editors April 7, 2023; accepted for publication (in revised form) November 28, 2023; published electronically February 8, 2024.

https://doi.org/10.1137/23M1564365

[†]Department of Mathematical Sciences, Worcester Polytechnic Institute, Worcester, MA 01609 USA (vdruskin1@gmail.com).

[‡]Department of Mathematics, Drexel University, Philadelphia, PA 19104 USA (moskow@math.drexel.edu).

[§]Schlumberger-Doll Research Center, Cambridge, MA 02139-1578 USA, and Department of Mathematics, Southern Methodist University, Dallas, TX 75205 USA (mzaslavsky@slb.com, mzaslavskiy@smu.edu).

[17, 16, 8, 9, 6, 14, 10]. Then, the ROM is transformed to a sparse form (tridiagonal for single-input/single-output (SISO) problems; block tridiagonal for multiple-input/multiple-output (MIMO) problems) by Lanczos orthogonalization. This data-driven ROM, in this orthogonalized form, has entries for which their dependence on the unknown PDE coefficients is approximately linear [3, 17, 7, 5, 14]. This process is related to works of Marchenko, Gelfand, Levitan, and Krein on inverse spectral problems and to the idea of spectrally matched second order staggered finite-difference grids first introduced in [15] and first used for direct inversion in [2].

The data-driven ROM can be viewed as a Galerkin matrix [1]. The crucial step, first noticed in [17], is that the orthogonalized Galerkin basis depends very weakly on the unknown medium. In [6], it was shown that this basis allows one to generate internal solutions from boundary data only, and in [18], the data-generated internal solutions \mathbf{u}_p (corresponding to unknown coefficient p) were used in the Lippmann–Schwinger integral equation, yielding the so-called Lippmann–Schwinger–Lanczos (LSL) method. In [13, 12], this method was first used in the time domain.

The LSL method for the frequency-domain problems works as follows. Given data F_p corresponding to unknown p and background data F_0 , the Lippmann–Schwinger integral equation says that

$$(1.1) F_p - F_0 = -\langle u_0, pu_p \rangle,$$

where \langle , \rangle is an appropriate inner product on the domain, and where u_p and u_0 are the unknown and background internal solutions, respectively. We then use the data generated internal solution \mathbf{u}_p in place of u_p :

$$(1.2) F_p - F_0 \approx -\langle u_0, p\mathbf{u}_p \rangle.$$

Recall that \mathbf{u}_p is precomputed directly from the data without knowing p.

Although a ROM must be constructed from a full symmetric transfer function, the LSL approach allows for its application to more general data sets. In [19], we showed several examples with nonsymmetric data arrays. Here we consider the monostatic formulation, that is, the case where one has only the diagonal of the matrix transfer function. We are again capitalizing on the fact that the LSL algorithm does not necessarily require the full matrix transfer function [19]. The structure of our monostatic measurement array can be summarized with the help of Figure 1.1. The column and row numbers correspond, respectively, to the indices of the receivers (outputs) and transmitters (inputs). The conventional data-driven ROM requires data from all receivers for all transmitters (the full data set), that is, that the measurements are given by the full square matrix (Figure 1.1). We assume here that we have only the diagonal part. We construct a separate ROM for each transmitter to obtain its corresponding internal field. Subsequently, all data will be coupled via the Lippmann–Schwinger equation. We show that even with this sparse data array, we retain some of the good performance of the ROM approach for strong nonlinear scattering, where the Born approximation fails.

Somewhat independently of the extension of LSL to monostatic problems, we present a simplification of the generation of the internal solutions in the time domain. In the spectral

Figure 1.1. Data arrays structures: Full MIMO square transfer function (data from all sources at all receivers) (left) versus monostatic data (data received only back at each source, typical of SARs) (right).

domain version [5, 18, 19], one would compute the mass matrix and stiffness matrix from the data, execute the Lanczos algorithm to orthogonalize, and then use the ROM as a forward operator to generate internal solutions. In the time domain, it turns out that we can obtain the same internal solutions directly from the mass matrix, with no need to introduce finite difference time stepping or the stiffness matrix. The formula we obtain offers the potential to speed up the computation and allows us to present the process more compactly.

This paper is organized as follows. In section 2 we describe the entire time domain process in detail for a one-dimensional single-input/single-output (SISO) problem including numerical experiments. A brief discussion of this simplified process for MIMO arrays in higher dimensions is described in section 3. Section 4 contains a detailed exposition of the monostatic formulation, and section 5 contains numerical experiments.

2. One-dimensional problem.

2.1. Statement of inverse problem. Consider the following one-dimensional model problem:

$$(2.1) u_{tt} + Au = 0 \text{ in } \Omega \times [0, \infty),$$

$$(2.2) u(t=0) = g \text{ in } \Omega,$$

(2.3)
$$u_t(t=0) = 0 \text{ in } \Omega,$$

where $\Omega = (0, 1)$, operator

$$(2.4) A = A_0 + q,$$

where $A_0 \ge 0$ is known, (for example, $A_0 = -\Delta$), $q(x) \ge 0$ is our unknown potential, and initial data is given by

(2.5)
$$g(x) = \sqrt{\hat{f}(\sqrt{A})}\delta_0(x)$$

for $\hat{f}(\omega)$, the Fourier transform of the initial pulse, which in our case we choose to be modulated Gaussian

(2.6)
$$f(t) = e^{-\sigma^2 t^2/2} \cos(\omega_0 t).$$

We also assume homogeneous Neumann boundary conditions on the spatial boundary $\partial\Omega$. The exact forward solution to (2.1) is

(2.7)
$$u(x,t) = \cos(\sqrt{A}t)g(x).$$

Of course this is unknown for our inverse problem, except near the receiver. We measure data at x = 0 at the 2n - 1 evenly spaced time steps $t = k\tau$ for k = 0, ..., 2n - 2 integrated against g:

(2.8)
$$F(k\tau) = \int_{\Omega} g(x) \cos(\sqrt{Ak\tau}) g(x) dx.$$

Recall that g is concentrated near x = 0, representing both source and receiver. The inverse problem is as follows: Given

$$\{F(k\tau)\}\$$
for $k = 0, \dots, 2n - 2,$

reconstruct q.

Remark 2.1. The initial data g is chosen in the form (2.5) for convenience; without the outer square root in the definition of g, the problem (2.1) is equivalent to having zero initial data and source term $\delta_0(x)f(t)$. Furthermore, for our choice of pulse f, we have

(2.9)
$$\hat{f}(\omega) = \frac{\sqrt{\pi}}{\sqrt{2}\sigma} \left(e^{-\frac{(\omega - \omega_0)^2}{2\sigma^2}} + e^{-\frac{(\omega + \omega_0)^2}{2\sigma^2}} \right),$$

so that for $\omega_0 = 0$

(2.10)
$$g = \left(\frac{\sqrt{2\pi}}{\sigma}\right)^{1/2} e^{-\frac{A}{2\sigma^2}} \delta_0(x)$$

is the solution of a time domain diffusion equation with operator A at time $\frac{1}{2\sigma^2}$, which is assumed to be early enough that our operator A is still equal to our known A_0 . The square root in the definition of g is chosen for symmetry reasons, which we will see below.

2.2. Mass matrix. Define u_k to be the true snapshot $u_k = u(k\tau, x)$ for $k = 0, \dots, 2n - 2$. Then the $n \times n$ mass matrix is defined by

$$(2.11) M_{kl} = \int_{\Omega} u_k u_l dx$$

for k, l = 0, ..., n - 1. From our expression (2.7) for the exact solution,

(2.12)
$$M_{kl} = \int_{\Omega} g(x) \cos(\sqrt{Ak\tau}) \cos(\sqrt{Al\tau}) g(x) dx.$$

The cosine angle sum formula

$$\cos\left(\sqrt{A}k\tau\right)\cos\left(\sqrt{A}l\tau\right) = \frac{1}{2}\left(\cos\left(\sqrt{A}(k-l)\tau\right) + \cos\left(\sqrt{A}(k+l)\tau\right)\right)$$

along with (2.8) gives us directly that

(2.13)
$$M_{kl} = \frac{1}{2} \left(F((k-l)\tau) + F((k+l)\tau) \right),$$

that is, we can obtain this mass matrix directly from the data. Note that we need precisely the 2n-1 data points corresponding to $k=0,\ldots,2n-2$ to obtain this $n\times n$ mass matrix.

2.3. Orthogonalization. Note that M is positive definite, so we can compute its Cholesky decomposition

$$M = U^{\top}U$$
,

where U is upper triangular. This would give us an orthogonalization of the true snapshots, if we knew them, as follows. Define \vec{u} to be a row vector of the first n snapshots corresponding to $k = 0, \ldots, n-1$, and set

$$(2.14) \vec{v} = \vec{u}U^{-1},$$

that is, we set

$$(2.15) v_k = \sum_{l} u_l U_{lk}^{-1}.$$

Then the set of functions $\{v_k\}$ will be orthonormal in the L^2 norm. One can check

$$\int_{\Omega} v_i v_j dx = \int_{\Omega} \left(\sum_{l} U_{li}^{-1} u_l \right) \left(\sum_{k} U_{kj}^{-1} u_k \right) dx
= \sum_{lk} U_{li}^{-1} U_{kj}^{-1} \int_{\Omega} u_l u_k dx
= \sum_{lk} U_{li}^{-1} U_{kj}^{-1} M_{lk}
= \sum_{lkr} U_{li}^{-1} U_{kj}^{-1} U_{lr}^{-1} U_{rk}
= \delta_{ij}.$$

Since U^{-1} is upper triangular, this procedure is precisely Gram–Schmidt performed on the true snapshots, in order of the time steps. That is, although we do not know the true snapshots, the mass matrix, obtained directly from the data, gives the transformation that orthogonalizes them.

2.4. Background problem. We now do all of the above for the known background problem, which has exact solution

(2.16)
$$u^{0}(x,t) = \cos(\sqrt{A_{0}}t)g(x).$$

We have the corresponding background snapshots $\{u_i^0\}$, mass matrix

(2.17)
$$M_{kl}^{0} = \int_{\Omega} u_k^0 u_l^0 dx,$$

corresponding Cholesky decomposition

$$M^0 = (U^0)^\top U^0,$$

and orthogonalized background snapshots

$$(2.18) \vec{v}^0 = \vec{u}^0 (U^0)^{-1}.$$

2.5. Crucial step. It was noticed in [17] that the *orthogonalized* snapshots depend very weakly on q. That is,

$$(2.19) \vec{v} \approx \vec{v}^0.$$

The reason why is that since we are doing Gram-Schmidt (2.15) on the time snapshots in sequential order, we are orthogonalizing away any reflections, since they are overlapping in space with previous times. A rigorous analysis for a related problem for a so-called optimal grid is given in [4]. The Gram-Schmidt procedure (2.15) is closely related to the Marchenko-Gelfand-Levitan setting, which will be examined more fully later.

2.6. Data-driven internal solutions. From (2.14) and (2.19) we have that the true snapshots

$$\vec{u} = \vec{v}U$$

 $\approx \vec{v}^0 U.$

This motivates the definition of our data generated snapshots

(2.20)
$$\vec{\mathbf{u}} = \vec{v}^0 U \\ = \vec{u}^0 (U^0)^{-1} U.$$

Note that in the right-hand side above we needed only the background solutions and the true U, which we obtained just from data. Equation (2.20) is a simple formula for the data generated internal solutions. In Figure 2.1 we illustrated how accurately $\vec{\mathbf{u}}$ approximates true snapshots \vec{u} and how different both are compared to the background snapshots \vec{u}^0 . Here we probed a medium with one bump (see top left in Figure 2.1 by modulated Gaussian waveform (2.9) with $\frac{\omega_0}{\sqrt{\sigma}} = 3$ excited and measured at x = 0. As one can expect, all three snapshots are on top of each other for small times when the waveform hadn't yet reached the reflector (see top right in Figure 2.1). In turn, for later times the background snapshots become totally different from the true snapshots; however, the latter are still reproduced by ROM-generated snapshots $\vec{\mathbf{u}}$ quite accurately (see bottom left and bottom right in Figure 2.1).

2.7. Inversion using Lippmann–Schwinger–Lanczos. For each time step $k\tau$, $k=0,\ldots, n-1$, consider the time domain Lippmann–Schwinger equation (see, for example, [11])

(2.21)
$$\frac{dF_0}{dt}(k\tau) - \frac{dF}{dt}(k\tau) = \int_0^{k\tau} \int_{\Omega} u_0(x, k\tau - t)u(x, t)q(x)dxdt.$$

Here we assume that derivative $\frac{dF}{dt}$ of the transfer function F is accessible at times $\{k\tau\}_{k=0}^{n-1}$. It can be obtained in a stable way if the Fourier image of the transfer function is available. Recall that for the Born approximation one would replace u(x,t) with the background $u_0(x,t)$ in the integral above. We instead replace u by its (time semidiscretized) data generated approximation $\vec{\mathbf{u}}$ from (2.20). Let $\mathbf{u}(x,t)$ be a time interpolant of $\vec{\mathbf{u}}$ to produce the LSL equation

(2.22)
$$\frac{dF_0}{dt}(k\tau) - \frac{dF}{dt}(k\tau) = \int_0^{k\tau} \int_{\Omega} u_0(x, k\tau - t) \mathbf{u}(x, t) q(x) dx dt,$$

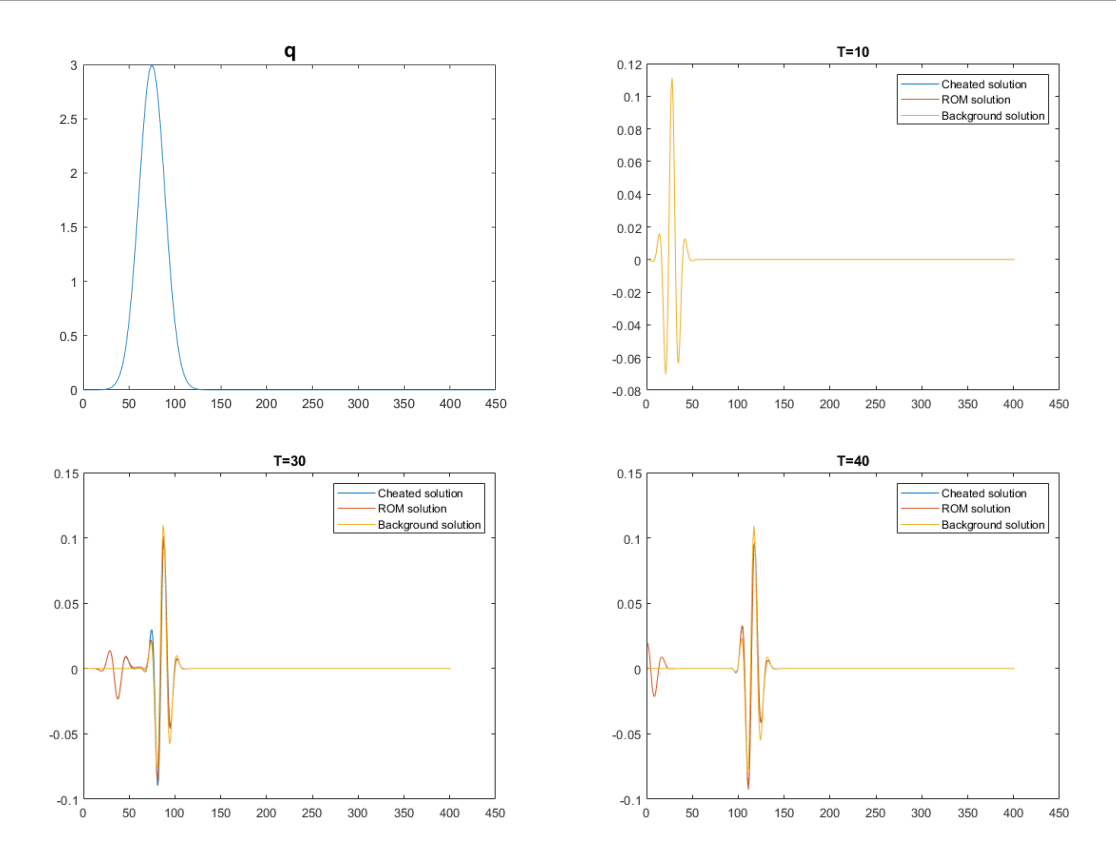


Figure 2.1. Data generated internal snapshots compared to the true snapshots and the background snapshots. Before hitting the scatterer, all overlap. After hitting the scatterer, the data generated solutions show reflections very close to the true ("cheated") solutions, while the background solutions are quite different.

which can be inverted for q. We note that instead of interpolating the snapshots in time, equivalently one may use the discrete time steps as nodes in some numerical approximation of (2.21).

2.8. Remarks on the relation to previous work. In [17], it was shown that snapshot u_i can be obtained by the action of the *i*th (first kind) Chebyshev polynomial of the propagation operator $P = \cos(\tau \sqrt{A})$ on the initial condition g. Hence the snapshots u_i form nested Krylov subspaces, that is,

$$\operatorname{span}\{u_0,\ldots,u_i\} = \operatorname{span}\{g,Pg,\ldots,P^ig\},$$

for all i = 0, ... n - 1. Therefore, Gram–Schmidt orthogonalization on the snapshots is equivalent to the Lanczos algorithm—hence the name Lippmann-Schwinger-Lanczos (LSL). The LSL algorithm was first introduced in [18], which was in the frequency domain, in which case the Lanczos algorithm is executed explicitly.

If one wants to compute a full ROM, we need a stiffness matrix too. The reconstruction methods in much of the previous work used the full ROM [17, 16, 9, 10]. We see here, though, that for time domain LSL, we need only the internal solutions, and hence only the mass matrix

M is needed, yielding the above algorithm simplification. There is also potential for speedup due to fast decay of the row elements of the upper triangular matrix $(U^0)^{-1}U$, potentially allowing for truncation. This is to be investigated in future work.

3. Full multidimensional problem: MIMO formulation. All of the above simplification extends to MIMO problems in higher dimensions. Consider

$$(3.1) u_{tt} + Au = 0 \text{ in } \Omega \times [0, \infty),$$

$$(3.2) u(t=0) = g \text{ in } \Omega,$$

(3.3)
$$u_t(t=0) = 0 \text{ in } \Omega,$$

where Ω is a domain in \mathbb{R}^d , and again operator $A = A_0 + q$. Consider the set of source/receivers modeled by $\{g_j\}$, a pulse localized near a receiver point x_j , and the response matrix

(3.4)
$$F^{ji}(k\tau) = \int_{\Omega} g_j(x) \cos(\sqrt{Ak\tau}) g_i(x) dx$$

for j, i = 1, ..., m, k = 0, ..., 2n - 1, representing the response at receiver j from source i at time $k\tau$. For the full MIMO problem, the mass tensor can again be obtained by the extension of (2.13) to blocks (as in many earlier works; see, for example, [11]), and the internal solutions again obtained from the block Cholesky (with $m \times m$ blocks) decomposition,

$$M = U^{\top}U$$
,

where U is block upper triangular. We note that there is some ambiguity in the choice of the blocks; we choose them so that all resulting orthogonalized functions

$$\vec{v} = \vec{u}U^{-1}$$

are mutually orthogonal. We do a similar decomposition/orthogonalization for the background mass matrix

$$M^0 = (U^0)^\top U^0, \quad \vec{v}^0 = \vec{u}^0 (U^0)^{-1}$$

to obtain the data generated internal solutions directly:

$$\vec{\mathbf{u}} = \vec{u}^0 (U^0)^{-1} U.$$

4. Monostatic formulation.

4.1. Linear-algebraic setup. For the synthetic aperture radar (SAR), we are given only the diagonal response

(4.1)
$$F^{jj}(k\tau) = \int_{\Omega} g_j(x) \cos(\sqrt{A}k\tau) g_j(x) dx$$

for j = 1, ..., m, k = 0, ..., 2n - 1, from which we are not able to obtain the complete mass matrix. However, we can instead compute a mass matrix and corresponding internal solution corresponding to each source separately.

Let $u^{(j)}$ be the true solution given data g_i . Define its set of snapshots

$$u_k^{(j)} = u^{(j)}(k\tau, x)$$

for k = 0, ..., 2n - 1, j = 1, ..., m to correspond to source j at time $k\tau$. For SARs this is read only at receiver j. Then the $n \times n$ mass matrix corresponding to this source is defined by

$$(4.2) M_{kl}^{(j)} = \int_{\Omega} u_k^j u_l^j dx$$

for k, l = 0, ..., n - 1. Again we have the expression (2.7) for the exact solution, and

(4.3)
$$M_{kl}^{(j)} = \int_{\Omega} g_j(x) \cos(\sqrt{Ak\tau}) \cos(\sqrt{Al\tau}) g_j(x) dx,$$

so the cosine angle formula and (4.1) give us directly that

(4.4)
$$M_{kl}^{(j)} = \frac{1}{2} \left(F^{jj} ((k-l)\tau) + F^{jj} ((k+l)\tau) \right).$$

Each $M^{(j)}$ is positive definite, so we can compute its Cholesky decomposition

$$M = (U^{(j)})^{\top} U^{(j)},$$

where each $U^{(j)}$ is upper triangular, for j = 1, ..., m. The orthogonalized true snapshots corresponding to source j are obtained in the exact same way,

(4.5)
$$\vec{v}^{(j)} = \vec{u}^{(j)} (U^{(j)})^{-1},$$

where $\vec{u}^{(j)}$ is the column vector of the original (yet unknown) snapshots. So we again have that

(4.6)
$$v_k^{(j)} = \sum_{l} u_l^{(j)} (U^{(j)})_{lk}^{-1},$$

and the set of functions $\{v_k^{(j)}\}$ for $k=0,1,\ldots,n-1$ will be orthonormal in the L^2 norm. We now do all of the above for the known background problem, which has exact solutions

(4.7)
$$u^{(j),0}(x,t) = \cos(\sqrt{A_0}t)g(x).$$

We have the corresponding background snapshots $\{u^{(j),0}\}$, mass matrices

$$M_{kl}^{(j),0} = \int_{\Omega} u_k^{(j),0} u_l^{(j),0} dx,$$

corresponding Cholesky decompositions

$$M^{(j),0} = (U^{(j),0})^{\top} U^{(j),0}$$

and orthogonalized background snapshots

(4.9)
$$\vec{v}^{(j),0} = \vec{u}^{(j),0} (U^{(j),0})^{-1}.$$

4.2. Crucial step. To accurately approximate the internal solution, we need an analogue of (2.19). It was shown in [17, 16] that (2.19) still holds for the MIMO formulation, provided we have sufficient array density and aperture. In contrast, the monostatic setup does not provide enough functions in the subspace to cancel all of the reflections from different directions during orthogonalization. However, it will still cancel the most important reflections, by the following reasoning.

Consider the 3D problem in the half-space, i.e., with $\Omega = (\mathbb{R}^3)^+$. Then for regular enough q and sharp pulse (small σ), we have that for a given source,

(4.10)
$$u(x,t) \approx \frac{1}{2\pi} \frac{\delta(\|x\| - t)}{\|x\|} + \eth(x,t),$$

where $\eth(x,t)$ is a smooth function satisfying the causality principle $\eth=0$ if $||x||\geq t$ and represents the difference from the background pulse. Thus the snapshots differ from the background spherically symmetric pulse by something with support in the region of the previous time snapshots. Thus the Gram-Schmidt orthogonalization against previous time pulses will approximately cancel *spherical averages* of $\eth(x,t)$, and the spherical averages of the orthogonalized snapshots should be close to the orthogonalized background snapshots. That is, for each $j=1,\ldots,m$,

(4.11)
$$\int_{\|x\|=const} \left[\vec{v}^{(j)} - \vec{v}^{(j),0} \right] \approx 0,$$

which means that the data generated internal solution is expected to have accurate spherical averages.

4.3. Data generated internal solutions. The formulas (4.5), (4.9), and (4.11) yield our data generated internal snapshots for each j,

(4.12)
$$\vec{\mathbf{u}}^{(j)} = \vec{v}^{(j),0} U^{(j)} \\ = \vec{u}^{(j),0} (U^{(j),0})^{-1} U^{(j)}.$$

These will approximate the true solution in the sense of averages on spheres centered at the transmitter/receiver location.

4.4. Monostatic Lippmann–Schwinger–Lanczos equation. We now consider the Lippmann–Schwinger equation. For each time step $k\tau$, $k=0,\ldots,n-1$, and for each source $j=1,\ldots,m$, we have

(4.13)
$$\frac{dF_0^{jj}}{dt}(k\tau) - \frac{dF^{jj}}{dt}(k\tau) = \int_0^{k\tau} \int_{\Omega} u^{(j),0}(x,k\tau - t)u^{(j)}(x,t)q(x)dxdt.$$

For the LSL method, we replace $u^{(j)}$ by its data generated approximation $\vec{\mathbf{u}}^{(j)}$ from (4.12), which we again need to interpolate. Let $\mathbf{u}^{(j)}(x,t)$ be a time interpolant of $\vec{\mathbf{u}}^{(j)}$ to produce the LSL equation

(4.14)
$$\frac{dF_0^{jj}}{dt}(k\tau) - \frac{dF^{jj}}{dt}(k\tau) = \int_0^{k\tau} \int_{\Omega} u^{(j),0}(x,k\tau - t)\mathbf{u}^{(j)}(x,t)q(x)dxdt$$

for j = 1, ..., m, k = 0, ..., n - 1, yielding nm equations to be inverted for q. The spheres discussed in the context of approximation (4.12) coincide with the slowness surfaces from the transmitter/receiver location. Thus the corresponding spherical waves give the dominant contribution in (4.13), and so it is reasonable to expect that (4.14) is a good approximation of (4.13). Below we will verify this reasoning via numerical experiments.

5. Numerical experiments. To simplify the generation of forward data, we present experiments with the near field setups, which can be generated by low flying drones. Here we show results for impermeable reflectors, for which (3.1) is known as a reasonable approximation. We start with the 2D inverse scattering problem to image 3 infinitely conductive reflectors shown on the top right in Figure 5.1. In this multi-scattering environment, it is highly challenging to reconstruct all of the details using SAR data only. We generate synthetic data by discretizing (3.1) in $\Omega = [0;300] \times [0;80]$ on a 600×160 grid and then solving the obtained equations for 27 sources emitting a nonmodulated Gaussian pulse. The Lippmann–Schwinger equation was approximated using quadrature on 300×80 grid. The Born solution captures the top boundaries of all three reflectors nicely; however, the bottom boundaries remain invisible. Also, the top reflector produced multiple ghost images (see top right plot in Figure 5.1). In turn, LSL managed not only to avoid that but also to exploit multiple scattering effects to map most of the bottom boundaries as well as the internal structure of the large reflectors (see bottom plot in Figure 5.1).

In the second numerical example we consider a so-called 2.5D SAR inverse scattering problem, that is, a 3D wave scattered by 2D reflectors. Here, we consider 2 thin elongated reflectors embedded in homogeneous background (see on the top left in Figure 5.2). For the SAR data collected along a single trajectory, this is a reasonable approximation that assumes that a medium is uniform in the horizontal direction perpendicular to the trajectory. To obtain synthetic data, we discretize (3.1) in $\Omega = [0; 100]^3$ using finite differences on a $200 \times 200 \times 200$ 3D grid. The obtained discrete problem was solved for 27 positions of radar that were emitting a nonmodulated Gaussian pulse (radar positions are marked by crosses in Figure 5.2). Then the Lippmann-Schwinger equation (4.14) is approximated using quadratures on a 100×100 2D grid. On the top right in Figure 5.2 we plot a cheated version of the Lippmann-Schwinger solution, i.e., when all internal solutions $u^{(j)}(x,t)$ are assumed to be known exactly. This corresponds to the best one could expect when solving (4.13) iteratively by updating the background solution computed from the approximate q obtained in the previous step. On the bottom two plots of Figure 5.2 we have shown the Born solution and the solution produced by our LSL approach, respectively. Due to the lack of aperture in SAR data, both approaches failed to image a part of the lower reflector. However, the Born solution also suffers from multiple ghost images of reflectors that are caused by the misinterpretation of multi-scattered effects. In turn, the LSL solution managed to clean out the multiple echoes and produced a significantly better image. In fact, this image is just slightly inferior to the one from the "cheated IE," which indicates good approximation of the interior solution.

¹Such an iterative Lippman–Schwinger (a.k.a. distorted Born method) would require multiple solutions of the forward problems, which can be prohibitively expensive for radar imaging, even if the iterations converge.

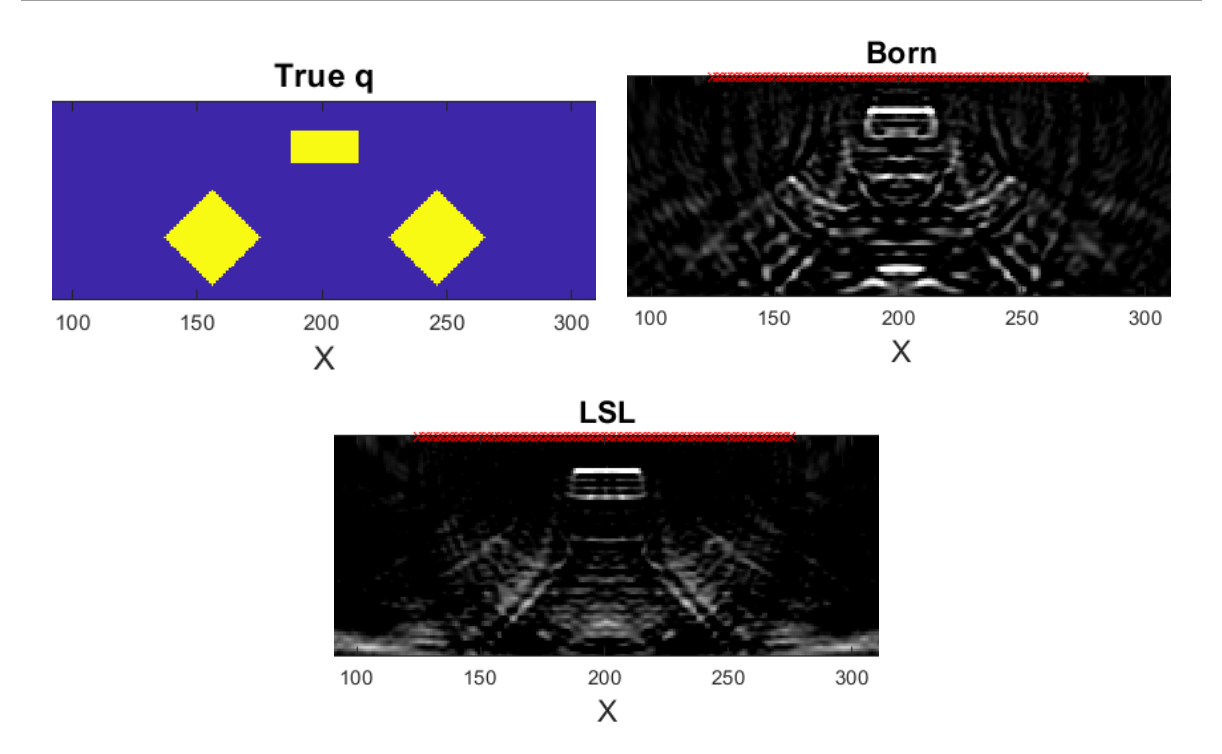


Figure 5.1. Numerical experiment 1: 2D inverse scattering problem with 3 massive reflectors. True medium (top left) and its reconstructions using the Born linearization (top right), and our LSL (bottom). The monostatic array locations are shown in red. We image the reflectivity distribution to map the boundaries of the reflectors. The LSL algorithm not only suppresses multiple echoes but also takes advantage of their illumination of some back sides of the reflectors. The noise seen at the periphery of the LSL image will be addressed in the future by improved processing.

In our final numerical experiment we consider a 2D inverse problem in the presence of variable wave speed c, assuming that the contrast targets are permeable by the primary waves. The forward problem can be formulated as

(5.1)
$$qu_{tt} + A_0 u = 0 \text{ in } \Omega \times [0, \infty),$$

$$(5.2) u(t=0) = g \text{ in } \Omega,$$

(5.3)
$$u_t(t=0) = 0 \text{ in } \Omega,$$

where Ω is a domain in \mathbb{R}^d and $q = \frac{1}{c^2}$. We note that in the 1D case this equation can be equivalently mapped to (2.1) via the Liouville transform in the travel-time coordinates. However, for multidimensional problems this is not possible, in a strict sense, due to distortion of the travel-time geodesics. One partial solution is to transform to travel-time coordinates in the dominant direction of propagation. This was done in the differential semblance method [22], and we plan to pursue this approach in our further work. Another approach is to iteratively update the internal solution in the seismic full wave inversion-type formulation, e.g., as was done in [13, 12]. However, this would not be feasible for SAR real time processing due to the cost of the forward problem solutions. Here we consider a simple approach which takes advantage of the fact that in radar applications, the waves propagate more slowly in the

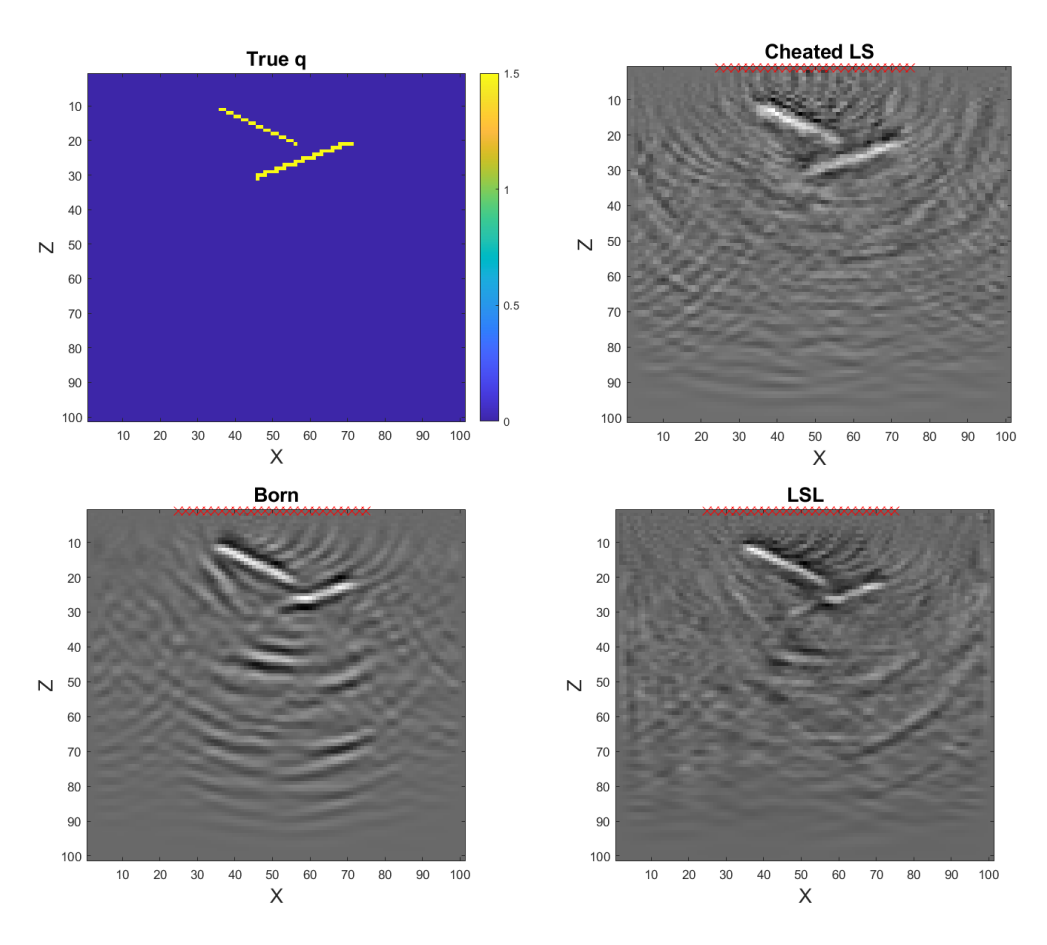


Figure 5.2. Numerical experiment 2: 2.5D inverse scattering problem with 2 elongated thin reflectors. True medium (top left) and its reconstructions using the cheated IE (top right), Born linearization (bottom left), and our LSL (bottom right). Similar to experiment 1, the monostatic array locations are shown in red.

targets than in the host medium (air). In this case the perturbations in the time snapshots have support in the region of the previous snapshots and can be canceled with orthogonalization. If the diameters of the perturbations are significantly smaller than their distance to the other objects, localized targets, even of high contrast, do not significantly disturb the first arrivals traveling in the fast background. The paths are mainly defined by inclusion shapes, and (2.1) qualitatively approximates wave propagation.

For a set of localized sources/receivers $\{g_j\}$, we define the SAR-type measurements

(5.4)
$$F^{jj}(k\tau) = \int_{\Omega} g_j(x)q(x)\cos\left(k\tau\sqrt{\frac{1}{q}A_0}\right)g_j(x)dx.$$

Here we assumed that q(x) is known at locations of sources/receivers. In principle, for imaging purposes, we could use the Lippmann–Schwinger equation earlier derived here for the for (3.1). However more accurate results are obtained if we use a formulation equivalent to (5.1). For each time step $k\tau$, k = 0, ..., n - 1, and for each source j = 1, ..., m we have the equation

(5.5)
$$\hat{F}_0^{jj}(k\tau) - \hat{F}^{jj}(k\tau) = \int_0^{k\tau} \int_{\Omega} u^{(j),0}(x,k\tau - t)u^{(j)}(x,t)q(x)dxdt,$$

where $\hat{F}(t) = \int_0^t F(s) ds$ and where $u^{(j),0}$ are snapshots of the solution of (5.1) for a known background coefficient $q = q_0$. Compared to the case (2.22) where $\frac{dF}{dt}$ was involved, here the Lippmann–Schwinger formulation requires the primitive \hat{F} of the transfer function F. In our experiments we computed it from F using quadratures. Similar to the case (2.22), in the LSL formulation we replace true internal solution $u^{(j)}(x,t)$ in the medium by its ROM approximant given by (4.12) where factors $U^{(j),0}$ and $U^{(j)}$ are obtained from Cholesky decompositions of mass matrices $M^{(j)} = \{M_{kl}^{(j)}\}_{k,l=0}^{n-1}$ and $M^{(j,0)} = \{M_{kl}^{(j,0)}\}_{k,l=0}^{n-1}$, and where

$$(5.6) M_{kl}^{(j)} = \int_{\Omega} g_j(x)q(x)\cos\left(k\tau\sqrt{\frac{1}{q(x)}A_0}\right)\cos\left(l\tau\sqrt{\frac{1}{q(x)}A_0}\right)g_j(x)dx,$$

and

(5.7)
$$M_{kl}^{(j),0} = \int_{\Omega} g_j(x) q_0(x) \cos\left(k\tau \sqrt{\frac{1}{q_0(x)}} A_0\right) \cos\left(l\tau \sqrt{\frac{1}{q_0(x)}} A_0\right) g_j(x) dx,$$

respectively.

In our numerical example we considered the same 2D medium as in the previous experiment (2 elongated reflectors within a homogeneous medium); however, the problem here is fully 2D, i.e., all of the traveling waves are 2D as well. To obtain synthetic data, we discretized (5.1) in $\Omega = [0, 1]^2$ using a 200×200 finite difference grid. We solved the discrete problem for 27 positions of a radar that was emitting a nonmodulated Gaussian pulse (radar locations are marked by crosses in Figure 5.3). The reflected wavefield was then recorded at those 27 positions. We discretized the Lippmann-Schwinger equation using a quadrature on a 100×100 grid. On the top right of Figure 5.3 we have shown a cheated solution that, as one can observe, reproduces the true model (see top left of Figure 5.3) quite accurately. In fact, for our model with slow inclusions, the true cheated wavefield is moving slowly through the reflectors. Hence, true snapshots provide a good resolution to image them—even better than for the case (2.22), which corresponds to a constant wavespeed. The bottom two plots correspond to Born (left) and LSL (right) solutions. Similar to the previous example, LSL managed to suppress many ghost images that are visible in the Born solution. However, the lack of aperture of SAR data didn't allow us to reconstruct the internal solutions accurately enough to perform on par with the cheated solution, which is in fact quantitatively accurate. This indicates that more improvement is possible with better approximation of the internal solution, for example, by using the first order reflectivity formulation [9], or combining the ROM with inverse Born series updates [21].

6. Conclusion. Conventional imaging of SAR data is based on the linearization of the underlying inverse scattering problem, i.e., the Born approximation. This approach, however, becomes unreliable in a multiple-scattering environment. To circumvent this problem, we considered a novel Lippmann–Schwinger formulation. The main drawback of the conventional Lippmann–Schwinger integral equation for the inverse scattering problem is that the interior solution used depends on the unknown PDE coefficient, making the problem nonlinear.

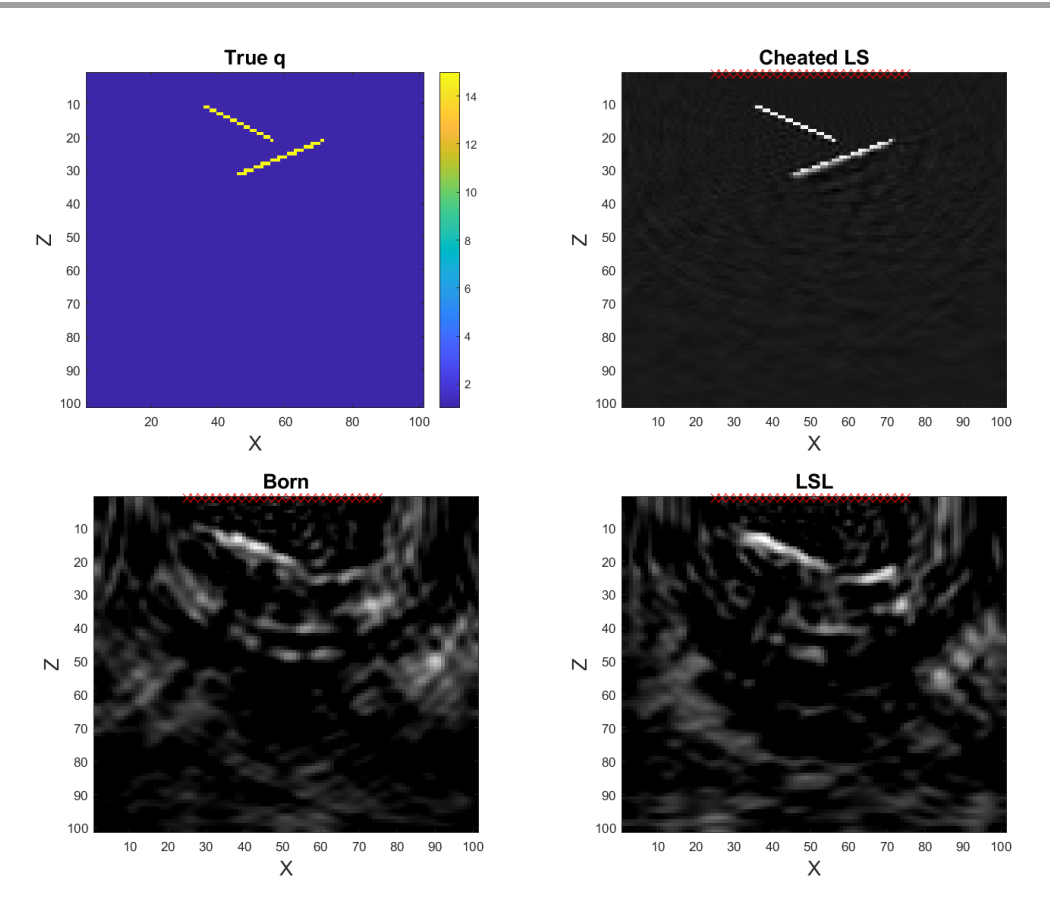


Figure 5.3. Numerical experiment 3: 2D inverse wave-speed problem with 2 elongated thin reflectors. True medium (top left) and its reconstructions using the cheated IE (top right), Born linearization (bottom left), and our LSL (bottom right). Monostatic array locations are shown in red.

Here we estimate the interior solution directly from the data with the help of the data-driven Gramian of the reduced order model (ROM), thus transforming the nonlinear Lippmann–Schwinger formulation to a linear one. Numerical examples for 2D and 2.5D (3D propagation and 2D reflectors) problems show a noticeable improvement compared to the linearized Born formulation.

In addition, our experiments reveal that the inversion results can be improved further by more accurate estimations of the internal solution. This could potentially be achieved by better parametrization of the inverse scattering problem (via first order formulations such as Maxwell's system), combining ROMs with the inverse Born series approach, and, for the case of a smoothly varying wave-speed, using a partial transformation to a travel time coordinate similar to the differential semblance method.

In our future work we also plan to investigate the effects of focusing, far field formulation, and excitation regimes commonly used in the radar community. Our long-term objective is to make the cost of the ROM approach comparable to the cost of the Born approximation. A bottleneck in the ROM approach is the efficient factorization of the data-driven Gramians,

and some promising results in this direction have already been obtained by the EPFL group following their earlier work on functions of Toeplitz matrices [20].

Acknowledgments. The authors are grateful to Liliana Borcea, Alex Mamonov, and Jörn Zimmerling for productive discussions that inspired this research.

REFERENCES

- [1] C. BEATTIE AND S. GUGERCIN, Model reduction by rational interpolation, in Model Reduction and Approximation: Theory and Algorithms, P. Benner, et al., Comput. Sci. Engrg. 15, SIAM, Philadelphia, 2017, pp. 297–334, https://doi.org/10.1137/1.9781611974829.ch7.
- [2] L. BORCEA AND V. DRUSKIN, Optimal finite difference grids for direct and inverse Sturm-Liouville problems, Inverse Problems, 18 (2002), pp. 979–1001, https://doi.org/10.1088/0266-5611/18/4/303.
- [3] L. BORCEA, V. DRUSKIN, F. GUEVARA VASQUEZ, AND A. V. MAMONOV, Resistor network approaches to electrical impedance tomography, in Inverse Problems and Applications: Inside Out II, Math. Sci. Res. Inst. Publ. 60, Cambridge University Press, Cambridge, UK, 2013, pp. 55–118.
- [4] L. BORCEA, V. DRUSKIN, AND L. KNIZHNERMAN, On the continuum limit of a discrete inverse spectral problem on optimal finite difference grids, Comm. Pure Appl. Math., 58 (2005), pp. 1231–1279.
- [5] L. BORCEA, V. DRUSKIN, A. MAMONOV, M. ZASLAVSKY, AND J. ZIMMERLING, Reduced order model approach to inverse scattering, SIAM J. Imaging Sci., 13 (2020), pp. 685–723, https://doi.org/10.1137/ 19M1296355.
- [6] L. BORCEA, V. DRUSKIN, A. V. MAMONOV, S. MOSKOW, AND M. ZASLAVSKY, Reduced order models for spectral domain inversion: Embedding into the continuous problem and generation of internal data, Inverse Problems, 36 (2020), 055010.
- [7] L. BORCEA, V. DRUSKIN, A. V. MAMONOV, AND M. ZASLAVSKY, A model reduction approach to numerical inversion for a parabolic partial differential equation, Inverse Problems, 30 (2014), 125011.
- [8] L. BORCEA, V. DRUSKIN, A. V. MAMONOV, AND M. ZASLAVSKY, Untangling nonlinearity in inverse scattering with data-driven reduced order models, Inverse Problems, 34 (2018), 065008.
- [9] L. BORCEA, V. DRUSKIN, A. V. MAMONOV, AND M. ZASLAVSKY, Robust nonlinear processing of active array data in inverse scattering via truncated reduced order models, J. Comput. Phys., 381 (2019), pp. 1–26.
- [10] L. Borcea, V. Druskin, and J. Zimmerling, A reduced order model approach to inverse scattering in lossy layered media, J. Sci. Comput., 89 (2021), pp. 1–36.
- [11] L. Borcea, J. Garnier, A. V. Mamonov, and J. Zimmerling, Waveform Inversion with a Data Driven Estimate of the Internal Wave, preprint, https://arxiv.org/abs/2208.11051, 2022.
- [12] L. Borcea, J. Garnier, A. V. Mamonov, and J. Zimmerling, Waveform inversion via reduced order modeling, Geophysics, (2023), pp. R175–R191, https://doi.org/10.1190/geo2022-0070.1.
- [13] L. BORCEA, J. GARNIER, A. V. MAMONOV, AND J. ZIMMERLING, Waveform inversion with a data driven estimate of the internal wave, SIAM J. Imaging Sci., 16 (2023), pp. 280–312, https://doi.org/10.1137/ 22M1517342.
- [14] L. BORCEA, J. GARNIER, A. V. MAMONOV, AND J. T. ZIMMERLING, Reduced Order Model Approach for Imaging with Waves, https://arxiv.org/abs/2108.01609, 2021.
- [15] V. DRUSKIN AND L. KNIZHNERMAN, Gaussian spectral rules for the three-point second differences: I. A two-point positive definite problem in a semi-infinite domain, SIAM J. Numer. Anal., 37 (1999), pp. 403–422, https://doi.org/10.1137/S0036142997330792.
- [16] V. DRUSKIN, A. MAMONOV, AND M. ZASLAVSKY, A nonlinear method for imaging with acoustic waves via reduced order model backprojection, SIAM J. Imaging Sci., 11 (2018), pp. 164–196, https://doi.org/ 10.1137/17M1133580.
- [17] V. DRUSKIN, A. V. MAMONOV, A. E. THALER, AND M. ZASLAVSKY, Direct, nonlinear inversion algorithm for hyperbolic problems via projection-based model reduction, SIAM J. Imaging Sci., 9 (2016), pp. 684–747, https://doi.org/10.1137/15M1039432.
- [18] V. DRUSKIN, S. MOSKOW, AND M. ZASLAVSKY, Lippmann-Schwinger-Lanczos algorithm for inverse scattering problems, Inverse Problems, 37 (2021), 075003, https://doi.org/10.1088/1361-6420/abfca4.

- [19] V. DRUSKIN, S. MOSKOW, AND M. ZASLAVSKY, On extension of the data driven ROM inverse scattering framework to partially nonreciprocal arrays, Inverse Problems, 38 (2022), 084002.
- [20] D. Kressner and R. Luce, Fast computation of the matrix exponential for a Toeplitz matrix, SIAM J. Matrix Anal. Appl., 39 (2018), pp. 23–47, https://doi.org/10.1137/16m1083633.
- [21] S. Moskow and J. C. Schotland, Convergence and stability of the inverse scattering series for diffuse waves, Inverse Problems, 24 (2008), 065005.
- [22] W. A. MULDER AND A. P. E. TEN KROODE, Automatic velocity analysis by differential semblance optimization, Geophysics, 67 (2002), pp. 1184–1191, https://doi.org/10.1190/1.1500380.